Monthly Notices of the ROYAL ASTRONOMICAL SOCIETY

MNRAS **507,** 4669–4683 (2021) https://doi.org/10.1093/mnras/stab2412
Advance Access publication 2021 August 24

Near-infrared spectroscopic indices for unresolved stellar populations – II. Index measurements

D. Gasparri [1★] L. Morelli,[1★] V. D. Ivanov,[2,3★] P. François,[4] A. Pizzella [5,6] L. Coccato,[2] E. M. Corsini [5,6] E. Dalla Bontà [5,6] L. Costantin[7,8] and M. Cesetti[9]

[1]*Instituto de Astronomía y Ciencias Planetarias, Universidad de Atacama, Copayapu 485, Copiapoó, Chile*
[2]*European Southern Observatory, Karl-Schwarzschild-Strasse 2, D-85748 Garching bei München, Germany*
[3]*European Southern Observatory, Avenida Alonso de Córdova 3107, Vitacura, Santiago, Chile*
[4]*GEPI, Observatoire de Paris, PSL Research University, CNRS, Université Paris Diderot, Sorbonne Paris Cité, 61 Avenue de l'Observatoire, F-75014 Paris, France*
[5]*Dipartimento di Fisica e Astronomia "G. Galilei", Università di Padova, vicolo dell'Osservatorio 3, I-35122 Padova, Italy*
[6]*INAF-Osservatorio Astronomico di Padova, vicolo dell'Osservatorio 5, I-35122 Padova, Italy*
[7]*Centro de Astrobiología (CSIC-INTA), Ctra de Ajalvir km 4, Torrejón de Ardoz, E-28850 Madrid, Spain*
[8]*INAF-Osservatorio Astronomico di Brera, via Brera 28, I-20121 Milano, Italy*
[9]*Independent Scholar, viale degli Aironi 4, I-30021 Caorle (VE), Italy*

Accepted 2021 August 17. Received 2021 July 22; in original form 2021 April 10

ABSTRACT

We measured the equivalent width of a large set of near-infrared (NIR, 0.8–2.4 μm) line-strength indices in XShooter medium-resolution spectra of the central regions of 14 galaxies. We found that two aluminum indices, Al at 1.31 μm and Al1 at 1.67 μm, and two CO indices, CO1 at 1.56 μm and CO4 at 1.64 μm, are tightly correlated with the velocity dispersion. Moreover, the NIR Al and CO1 indices show strong correlations with the optical Mg2 and Mgb indices, which are usually adopted as α/Fe-enhancement diagnostics. The molecular FeH1 index at 1.58 μm correlates tightly with the optical ⟨Fe⟩ and [MgFe]′ indices, which are used as total metallicity diagnostics. The NIR Paβ index at 1.28 μm has a behaviour similar to the optical Hβ index, which is a diagnostic of mean age. We defined two new composite indices, ⟨Al⟩ and [AlFeH], as possible candidates to be used as NIR diagnostics of total metallicity and α/Fe enhancement. The NIR ⟨Al⟩ index has a strong correlation with the optical Mg2 and Mgb indices, while the [AlFeH] index is tightly correlated with the optical ⟨Fe⟩ and [MgFe]′ indices. The distribution of the data points in the NIR Paβ–⟨Al⟩ and Paβ–[AlFeH] diagrams mimics that in the optical [MgFe]′–Hβ and Mgb–⟨Fe⟩ diagrams, which are widely used to constrain the properties of the unresolved stellar populations. We concluded that some NIR line-strength indices could be useful in studying stellar populations as well as in fine-tuning stellar population models.

Key words: surveys – galaxies: abundances – galaxies: formation – galaxies: stellar content – infrared: galaxies.

1 INTRODUCTION

Since the 1970s, when the modern era of galaxy spectroscopy began with the introduction of image intensifiers (e.g. the Image Dissector Scanner at Lick Observatory: Robinson & Wampler 1972), many advances in our knowledge of unresolved stellar populations have been made by investigating optical spectra of galaxies. Nowadays, line-strength index analysis (e.g. Worthey et al. 1994; Morelli et al. 2008; Vazdekis et al. 2010; Costantin et al. 2019) and full spectral fitting (e.g. Sarzi et al. 2006b; Koleva et al. 2009; Morelli et al. 2015) are standard tools to recover the star-formation history of galaxies.

Although some pioneering works on the strongest near-infrared (NIR, 0.8–2.4 μm) spectral absorption features date back to the 1990s (Silva et al. 1994; Origlia et al. 1997), only recently have the increasing size and efficiency of NIR detectors allowed a comprehensive spectroscopic study of the *IYJHK* bands, making the NIR domain complementary to the optical range in studying the stellar populations of galaxies. The need to observe the optical range at high redshifts triggered the building of a new generation of NIR-optimized spectrographs (e.g. Cuby et al. 2010; Mobasher, Crampton & Simard 2010; Cirasuolo et al. 2011), which also offers the chance to have high-quality data to investigate the NIR spectral energy distribution of nearby galaxies in detail.

This provides some advantages. For example, the luminosity fraction of stars of early spectral types diminishes as the wavelength increases (Bica 1988), and we can actually isolate asymptotic giant branch (AGB) and red giant branch (RGB) components. Indeed, the contribution of stars outside the AGB–RGB branches is negligible in the *K* band for all galaxies, independently of their Hubble type (Kotilainen et al. 2012). Nevertheless, the AGB and RGB phases are still poorly understood and very difficult to model in the NIR (Röck et al. 2017; Riffel et al. 2019). On the other hand, the reduced effect of reddening with respect to the optical range is a crucial advantage of NIR and it allows us to peer into highly obscured galaxies, otherwise impossible to investigate (Engelbracht et al. 1998; Ivanov et al. 2000). In this context, analysing NIR spectra could help us to understand better the connection between the presence of dust and young

★ E-mail: daniele.gasparri@postgrados.uda.cl (DG); lorenzo.morelli@uda.cl (LM); vivanov@eso.org (VDI)

stellar populations, as found for example by Peletier et al. (2007) in the central regions of early-type spirals. The major observational drawback for NIR spectroscopy is the strong contamination produced by telluric absorption and atmospheric emission lines, which overlap interesting spectral features of galaxies even at low redshift (François et al. 2019).

Different sets of NIR line-strength indices have been developed since the early 1980s (Jones, Alloin & Jones 1984; Bica & Alloin 1987; Cenarro et al. 2003), focusing mainly on the calcium triplet (CaT) and hydrogen Paschen lines (see Cenarro et al. 2001, for an extensive review).

Mannucci et al. (2001) investigated some NIR features, at low resolution ($300 < R < 600$) and facing severe line blending, in a sample of 28 nearby galaxies covering the entire Hubble sequence. Silva, Kuntschner & Lyubenova (2008) studied some *K*-band line-strength indices, including the strong CO molecular feature at 2.30 μm and Ca and Na indices, in a sample of 11 early-type galaxies in the Fornax cluster. Cesetti et al. (2009) performed low-resolution ($R = 1000$) spectroscopy of 14 early-type galaxies in the wavelength range 1.5–2.4 μm, covering the strong Mg feature at 1.50 μm. Kotilainen et al. (2012) focused on the strongest Mg, Si, and CO features detected in the central regions of a sample of 29 quiescent spiral galaxies, which they measured at a resolution of $R \sim 600$ in the *H* and *K* bands. Röck (2015) defined and investigated some new line-strength indices in the *JHK* bands, including those of the aluminium 1.30-μm line and other Mg lines. Riffel et al. (2019) measured several line-strength indices from *I* to *K* bands in 16 luminous infrared spiral galaxies observed at a resolution of $R = 1000$ and in 19 early-type galaxies from the literature.

With the increasing number and quality of NIR spectra, large stellar libraries have been assembled, either limited to the *JHK* bands (Ivanov et al. 2004) or covering the entire NIR range, like the NASA Infrared Telescope Facility (IRTF) spectral library (Rayner, Cushing & Vacca 2009; Villaume et al. 2017) and the more recent XShooter spectral library (XSL: Arentsen et al. 2019). These are the base for defining and calibrating new NIR line-strength indices and for building more complete and reliable single stellar population (SSP) models. The end products of the SSP models are spectra of single bursts of star formation at fixed age, metallicity, and abundance of α-elements (Röck et al. 2015, 2016; Vazdekis et al. 2016). If the assumption of a SSP or of dominating SSP is not valid (e.g. for E+A galaxies or for particular galaxy components), the SSP models can be combined with different luminosity or mass weights to mimic the spectra of multicomponent stellar populations (e.g. Cappellari & Emsellem 2004) and also to account for an additional gaseous component (e.g. Sarzi et al. 2006a). This can be done either using the typical line-strength indices (Mehlert et al. 2003; Sánchez-Blázquez et al. 2006) or by combining the analysis of a set of line-strength indices (e.g. Zibetti et al. 2017; Costantin et al. 2019), or through a full spectral fitting analysis (e.g. Morelli et al. 2013; Costantin et al. 2021).

This is a relatively new field of extragalactic research and it still lacks a reliable system of line-strength indices to be used as a diagnostic tools like the Lick/IDS ones (Faber et al. 1985; Worthey et al. 1994; Worthey & Ottaviani 1997; Thomas, Maraston & Bender 2003). With the aim of filling this void, in Cesetti et al. (2013) and Morelli et al. (2020) we developed a set of spectroscopic diagnostics for stellar physical parameters based on NIR spectral features in the wavelength range 0.8–5 μm.

In François et al. (2019), hereafter Paper I, we presented a sample of high signal-to-noise ratio (SNR) galaxy spectra obtained at medium resolution ($R \sim 4000-5000$) with the XShooter spectrograph (Guinouard et al. 2006) mounted at the Very Large Telescope (VLT) of the European Southern Observatory (ESO). These spectra map the optical and NIR ranges of the galaxy spectral energy distribution simultaneously, making the direct comparison of spectral properties of unresolved stellar populations in these regimes easier. The purpose of this work is to analyse these XShooter spectra, focusing on the NIR bands, to investigate the wide set of line-strength indices defined by Cesetti et al. (2013) and Morelli et al. (2020).

We structured the work as follows. We introduce our dataset in Section 2. We describe measurements of the NIR line-strength indices in Section 3. We investigate our final set of 40 NIR line-strength indices in Section 4 and show the correlations among the NIR line-strength indices and with the central velocity dispersion of the galaxies. We focus on age and metallicity indicators in Section 5 and show the correlations with the optical Lick/IDS line-strength indices. Finally, we discuss the results in Section 6 and present our conclusions in Section 7.

2 SPECTROSCOPIC DATA

Medium-resolution spectroscopy was performed performed with the UVB ($R \sim 4000$), VIS ($R \sim 5400$) and NIR ($R \sim 4300$) arms of the ESO XShooter spectrograph for a sample of 14 nearby galaxies (Prop. Id. 086.B-0900, PI: Cesetti, M.). The morphological type of the sample galaxies ranges from E to Sc, the central stellar velocity dispersion is between 36 and 335 km s^{-1}, and their distance is between 13 and 62 Mpc.

The spectra were obtained along the major axis of the galaxies and were co-added along the spatial direction to map a central region of 1.5×1.5 arcsec^2, which corresponds to an area ranging from 65×65 pc^2 to 430×430 pc^2 depending on distance, with a typical SNR$\sim$ 100 Å^{-1}. In Paper I, we measured the Mg, Fe, and Hβ line-strength indices of the Lick/IDS system (Faber et al. 1985; Worthey et al. 1994), ⟨Fe⟩ mean index (Gorgas, Efstathiou & Aragon Salamanca 1990), [MgFe]′ combined index (Thomas et al. 2003), and their uncertainties following Morelli et al. (2004, 2012, 2016). We derived the stellar population properties of the sample galaxies using the SSP models by Johansson, Thomas & Maraston (2010) and found that ages range from 0.8–15 Gyr and metallicities ([*Z*/H]) from −0.39 to +0.55 dex.

Considering the SNR, spatial and spectral resolution, and wavelength range of the spectra, as well as the Hubble type, age, and metallicity of the sample galaxies, our data have an unprecedented quality with respect to previous works and they represent an excellent resource for studying stellar populations in the NIR bands.

3 DEFINITION AND MEASUREMENT OF NIR LINE-STRENGTH INDICES

3.1 Line-strength index measurement

In the past 15 years, different authors have defined and tested an increasing set of NIR line-strength indices as possible diagnostic tools (e.g. Silva et al. 2008; Cesetti et al. 2009; Röck et al. 2015; Riffel et al. 2019, and references therein). Here, we adopted the definitions given by Cesetti et al. (2013) for the line-strength indices in the *I* and *K* bands and by Morelli et al. (2020) for the *Y*, *I*, and *H* bands, which rely on the concept of sensitivity maps to identify spectral features that are more sensitive to age and metallicity. Considering the spectral range of our data, we identified and measured 75 NIR

Table 1. The final set of 40 NIR line-strength indices investigated in this work.

Index name	Dominated by	Line limits (μm)	Blue continuum (μm)	Red continuum (μm)	Main Reference	Additional Reference
Pa1	H I (n=3)	0.8461–0.8474	0.8474–0.8484	0.8563–0.8577	2	
Ca1	Ca II	0.8484–0.8513	0.8474–0.8484	0.8563–0.8577	2	
Ca2	Ca II	0.8522–0.8562	0.8474–0.8484	0.8563–0.8577	2	
Ca3	Ca II	0.8642–0.8682	0.8619–0.8642	0.8700–0.8725	2	
Mgi	Mg I	0.8802–0.8811	0.8776–0.8792	0.8815–0.8850	3	
Ti	Ti I	0.9780–0.9795	0.9750–0.9760	0.9800–0.9810	1	
FeH	FeH	0.9900–0.9950	0.9840–0.9850	0.9985–0.9995	1	9,10
Paδ	H I	1.0040–1.0067	1.0020–1.0030	1.0067–1.0077	1	
FeTi	Fe I, Ti I	1.0390–1.0408	1.0198–1.0210	1.0438–1.0446	1	
CN	CN	1.0868–1.0882	1.0640–1.0650	1.0892–1.0902	1	
Sr	Sr II	1.0913–1.0923	1.0892–1.0902	1.0978–1.0988	1	
K1A	K I	1.1670–1.1714	1.1560–1.1585	1.1716–1.1746	1	9,10
K1B	K I	1.1765–1.1800	1.1716–1.1746	1.1805–1.1815	1	9,10
Mgj	Mg I	1.1820–1.1840	1.1805–1.1815	1.1855–1.1875	1	7
Sij	Si I	1.1977–1.2004	1.1910–1.1935	1.2050–1.2070	1	
SiMg	Si I, Mg I	1.2070–1.2095	1.2050–1.2070	1.2050–1.2070	1	
K2A	K I	1.2415–1.2455	1.2350–1.2380	1.2460–1.2490	1	7,10
Paβ	H I	1.2795–1.2840	1.2755–1.2780	1.2855–1.2873	1	
Al	Al I	1.3115–1.3168	1.3050–1.3075	1.3230–1.3250	1	9,11
Mg1h	Mg I	1.4850–1.4910	1.4830–1.4850	1.4910–1.5000	1	7
Mg2h	Mg I	1.5000–1.5080	1.4910–1.5000	1.5100–1.5120	1	7,4
CO1	^{12}CO(2,0)	1.5570–1.5635	1.5480–1.5500	1.5930–1.5940	1	7
Br_{15}	H I	1.5670–1.5720	1.5480–1.5500	1.5930–1.5940	1	
Mg3h	Mg I	1.5730–1.5800	1.5480–1.5500	1.5930–1.5940	1	7
FeH1	FeH	1.5820–1.5860	1.5480–1.5500	1.5930–1.5940	1	4,7,8
Sih	Si I	1.5870–1.5910	1.5480–1.5500	1.5930–1.5940	1	4,7,8
CO2	^{12}CO(2,0)	1.5950–1.6000	1.5930–1.5940	1.6160–1.6180	1	7
CO3	^{12}CO(2,0)	1.6180–1.6220	1.6160–1.6180	1.6340–1.6370	1	8
CO4	^{12}CO(2,0)	1.6390–1.6470	1.6340–1.6370	1.6585–1.6605	1	
Fe3	Fe I	1.6510–1.6580	1.6340–1.6370	1.6585–1.6605	1	
Al1	Al I	1.6705–1.6775	1.6585–1.6605	1.6775–1.6790	1	
COMg	^{12}CO(2,0), Mg I	1.7050–1.7130	1.6920–1.6960	1.7140–1.7160	1	4
Br_{10}	H I	1.7350–1.7390	1.7250–1.7280	1.7440–1.7480	1	
Mg1k	Mg I	2.1040–2.1110	2.1000–2.1040	2.1110–2.1150	4	
Nadk	Na I	2.2000–2.2140	2.1934–2.1996	2.2150–2.2190	6	
FeA	Fe I	2.2250–2.2299	2.2133–2.2176	2.2437–2.2497	5	
FeB	Fe I	2.2368–2.2414	2.2133–2.2176	2.2437–2.2497	5	
Ca_d	Ca I	2.2594–2.2700	2.2516–2.2590	2.2716–2.2888	6	
Mg2k	Mg I	2.2795–2.2845	2.2700–2.2720	2.2850–2.2874	5	
CO12	^{12}CO(2,0)	2.2910–2.3070	2.2516–2.2590	2.2716–2.2888	3	

Note. The references are: 1 = Morelli et al. (2020); 2 = Cenarro et al. (2001); 3 = Cesetti et al. (2013); 4 = Ivanov et al. (2004); 5 = Silva et al. (2008); 6 = Cesetti et al. (2009); 7 = Riffel et al. (2019); 8 = Origlia, Moorwood & Oliva (1993); 9 = Conroy & van Dokkum (2012), Villaume et al. (2017); 10 = McLean et al. (2003), Cushing, Rayner & Vacca (2005); 11 = Röck et al. (2015).

line-strength indices. This is one of the largest and most complete sets of NIR line-strength indices investigated so far.

For each sample galaxy, we measured the equivalent width (EW) of all the above NIR line-strength indices as done by Cesetti et al. (2013) and Morelli et al. (2020) for the IRTF stellar library. In this work, we adopted the same spatial aperture used for the measuring the optical line-strength indices in Paper I. We measured the SNR of each NIR line-strength index in two adjacent continuum bands. Ten out of 14 galaxies have SNR $>$ 100 Å^{-1} for all the line-strength indices, whereas the line-strength indices of NGC 3423, NGC 4415, and NGC 7424 have SNR $<$ 30 SNR Å^{-1}. In the case of NGC 1600, contamination due to the residuals of sky subtraction prevented us from measuring all the NIR line-strength indices. The errors in indices were derived from photon statistics and CCD readout noise, and calibrated by means of Monte Carlo simulations. For each line-strength index in each spectrum, we generated 1000 simulations.

We corrected the EWs to zero velocity dispersion following the method of Silva et al. (2008) and Cesetti et al. (2009). We broadened the spectra of the giant stars with spectral type ranging from K0–M3 in the IRTF library up to 400 km s^{-1} with bins of 50 km s^{-1}. For each NIR line-strength index, we calculated the correction coefficients with a spline interpolation of the average broadened EW. In addition, as a sanity check we considered different samples of stars including supergiant stars and/or extending to late G-type stars, and considering stellar spectra from the XSL. The correction coefficients are consistent within the uncertainties and match those calculated by Cesetti et al. (2013) and Morelli et al. (2020) for giant K-type stars. The uncertainties in the correction coefficients were estimated following a similar approach to the coefficient determination. We calculated the root-mean-square (rms) of the EW of the stellar spectra with respect to the mean values for any velocity-dispersion broadening value of any NIR line-strength

Table 2. The equivalent widths in Å of the NIR line-strength indices of the sample galaxies with high SNR ($>$ 100 Å^{-1}).

Index	NGC 584	NGC 636	NGC 897	NGC 1357	NGC 1425	NGC 1700	NC2613	NGC 3115	NGC 3377	NGC 3379
Pa1	0.50 ± 0.12	0.56 ± 0.10	0.52 ± 0.13	0.45 ± 0.07	0.35 ± 0.05	0.19 ± 0.06	0.52 ± 0.09	1.04 ± 0.25	0.44 ± 0.07	0.50 ± 0.12
Ca1	1.40 ± 0.12	1.49 ± 0.09	1.49 ± 0.14	1.44 ± 0.07	1.46 ± 0.05	1.37 ± 0.13	1.38 ± 0.08	1.23 ± 0.14	1.46 ± 0.07	1.41 ± 0.13
Ca2	3.42 ± 0.08	3.61 ± 0.06	3.60 ± 0.08	3.57 ± 0.05	3.67 ± 0.04	–	3.43 ± 0.06	3.44 ± 0.08	3.59 ± 0.05	3.31 ± 0.07
Ca3	2.46 ± 0.05	3.15 ± 0.04	2.89 ± 0.06	3.12 ± 0.04	3.14 ± 0.03	–	3.15 ± 0.05	2.97 ± 0.07	3.05 ± 0.04	2.87 ± 0.05
Mgi	0.36 ± 0.06	0.72 ± 0.06	0.53 ± 0.07	0.73 ± 0.05	0.64 ± 0.04	1.37 ± 0.13	0.72 ± 0.06	0.54 ± 0.05	0.55 ± 0.04	0.88 ± 0.07
Ti	0.61 ± 0.04	0.53 ± 0.04	0.59 ± 0.04	0.58 ± 0.03	0.62 ± 0.05	−0.07 ± 0.03	0.75 ± 0.04	−0.33 ± 0.20	0.26 ± 0.05	0.88 ± 0.13
FeH	1.56 ± 0.34	0.94 ± 0.21	2.02 ± 0.45	1.04 ± 0.20	0.81 ± 0.14	3.15 ± 0.75	1.01 ± 0.21	0.55 ± 0.22	0.59 ± 0.12	−0.08 ± 0.07
Paδ	0.75 ± 0.11	0.63 ± 0.10	0.83 ± 0.13	0.52 ± 0.07	0.82 ± 0.07	0.90 ± 0.12	0.52 ± 0.12	0.84 ± 0.13	0.77 ± 0.09	0.66 ± 0.12
FeTi	0.41 ± 0.04	0.40 ± 0.04	0.28 ± 0.03	0.24 ± 0.03	0.22 ± 0.04	0.34 ± 0.03	0.10 ± 0.02	0.37 ± 0.03	0.34 ± 0.03	0.34 ± 0.03
CN	0.62 ± 0.05	0.62 ± 0.04	0.54 ± 0.05	0.43 ± 0.03	0.41 ± 0.03	0.62 ± 0.05	0.50 ± 0.03	0.56 ± 0.06	0.52 ± 0.03	0.59 ± 0.04
Sr	−0.14 ± 0.04	−0.13 ± 0.03	−0.10 ± 0.04	−0.23 ± 0.04	−0.13 ± 0.02	−0.11 ± 0.03	−0.03 ± 0.02	−0.14 ± 0.04	−0.15 ± 0.03	−0.14 ± 0.04
K1A	0.67 ± 0.06	0.48 ± 0.05	0.34 ± 0.04	0.40 ± 0.04	0.79 ± 0.04	0.49 ± 0.05	0.75 ± 0.04	0.46 ± 0.09	0.26 ± 0.05	0.60 ± 0.09
k1B	0.66 ± 0.05	−0.28 ± 0.04	0.90 ± 0.06	0.28 ± 0.04	0.20 ± 0.05	1.07 ± 0.06	0.83 ± 0.05	1.01 ± 0.09	1.23 ± 0.06	0.69 ± 0.05
Mgj	1.17 ± 0.07	0.28 ± 0.05	1.26 ± 0.07	0.87 ± 0.07	1.72 ± 0.21	1.16 ± 0.06	0.93 ± 0.08	1.12 ± 0.12	1.27 ± 0.07	1.03 ± 0.08
Sij	0.89 ± 0.06	1.06 ± 0.06	1.09 ± 0.07	0.98 ± 0.06	0.87 ± 0.04	0.89 ± 0.05	0.84 ± 0.05	0.63 ± 0.06	1.02 ± 0.05	0.84 ± 0.05
SiMg	0.59 ± 0.04	0.57 ± 0.04	0.51 ± 0.05	0.61 ± 0.05	0.57 ± 0.03	0.45 ± 0.03	0.69 ± 0.05	0.28 ± 0.05	0.46 ± 0.04	0.42 ± 0.06
K2A	1.06 ± 0.04	0.99 ± 0.04	1.44 ± 0.06	1.02 ± 0.03	0.57 ± 0.02	0.69 ± 0.03	0.81 ± 0.03	1.07 ± 0.04	0.91 ± 0.02	0.97 ± 0.03
Paβ	1.94 ± 0.08	1.99 ± 0.08	1.52 ± 0.08	1.63 ± 0.07	1.69 ± 0.05	1.80 ± 0.08	1.98 ± 0.08	1.72 ± 0.08	1.67 ± 0.06	1.56 ± 0.07
Al	1.99 ± 0.08	1.54 ± 0.06	1.83 ± 0.08	1.72 ± 0.06	1.04 ± 0.02	2.05 ± 0.11	1.58 ± 0.05	2.04 ± 0.09	1.53 ± 0.07	2.04 ± 0.09
Mg1h	1.48 ± 0.38	1.75 ± 0.38	1.57 ± 0.43	1.73 ± 0.32	1.58 ± 0.22	1.93 ± 0.53	1.28 ± 0.25	1.91 ± 0.61	1.78 ± 0.37	1.72 ± 0.47
Mg2h	4.26 ± 0.20	4.44 ± 0.16	4.34 ± 0.24	4.47 ± 0.15	3.89 ± 0.10	4.39 ± 0.23	4.31 ± 0.14	4.44 ± 0.32	4.45 ± 0.17	3.70 ± 0.23
CO1	5.02 ± 0.21	4.99 ± 0.19	5.23 ± 0.23	4.38 ± 0.18	4.10 ± 0.16	4.61 ± 0.20	4.32 ± 0.20	5.21 ± 0.23	4.87 ± 0.19	5.14 ± 0.22
Br15	1.46 ± 0.28	1.96 ± 0.31	1.85 ± 0.39	1.75 ± 0.26	1.38 ± 0.18	1.69 ± 0.34	1.44 ± 0.25	1.24 ± 0.29	0.93 ± 0.17	1.95 ± 0.39
Mg3h	7.20 ± 0.31	6.61 ± 0.27	6.20 ± 0.29	6.68 ± 0.27	6.11 ± 0.23	6.34 ± 0.28	5.76 ± 0.26	6.64 ± 0.31	5.75 ± 0.24	6.40 ± 0.29
FeH1	2.64 ± 0.24	2.41 ± 0.20	2.52 ± 0.26	2.47 ± 0.20	2.54 ± 0.18	2.12 ± 0.21	1.94 ± 0.19	2.56 ± 0.27	2.06 ± 0.18	2.56 ± 0.25
Sih	4.59 ± 0.16	4.15 ± 0.15	4.48 ± 0.17	4.15 ± 0.15	4.48 ± 0.15	4.20 ± 0.15	4.42 ± 0.17	4.39 ± 0.15	3.96 ± 0.14	4.29 ± 0.16
CO2	3.55 ± 0.27	3.67 ± 0.24	3.34 ± 0.24	3.76 ± 0.19	3.47 ± 0.16	3.56 ± 0.25	3.29 ± 0.20	3.41 ± 0.29	2.71 ± 0.17	3.09 ± 0.21
CO3	4.85 ± 0.19	4.52 ± 0.18	4.69 ± 0.18	4.94 ± 0.20	4.50 ± 0.16	4.11 ± 0.18	4.27 ± 0.18	3.98 ± 0.17	4.55 ± 0.17	3.74 ± 0.15
CO4	3.80 ± 0.08	4.27 ± 0.08	4.22 ± 0.09	3.77 ± 0.09	3.94 ± 0.08	4.14 ± 0.08	3.30 ± 0.07	4.31 ± 0.10	4.47 ± 0.08	4.02 ± 0.08
Fe3	−0.20 ± 0.07	0.62 ± 0.12	0.99 ± 0.23	1.17 ± 0.20	0.19 ± 0.06	0.81 ± 0.19	0.35 ± 0.08	0.48 ± 0.16	1.13 ± 0.18	0.21 ± 0.08
Al1	4.05 ± 0.38	3.88 ± 0.24	4.42 ± 0.39	3.64 ± 0.17	3.39 ± 0.23	3.43 ± 0.31	3.44 ± 0.21	4.45 ± 0.50	4.08 ± 0.21	4.11 ± 0.41
COMg	5.25 ± 0.12	5.16 ± 0.11	4.71 ± 0.11	5.22 ± 0.12	5.18 ± 0.10	4.59 ± 0.11	5.01 ± 0.11	4.99 ± 0.12	5.02 ± 0.11	4.95 ± 0.11
Br10	1.24 ± 0.09	1.16 ± 0.07	1.74 ± 0.11	1.25 ± 0.07	1.19 ± 0.06	1.45 ± 0.09	1.08 ± 0.07	1.32 ± 0.09	1.18 ± 0.08	1.13 ± 0.09
MgIk	2.02 ± 0.07	1.64 ± 0.06	1.81 ± 0.07	1.77 ± 0.07	1.08 ± 0.05	1.56 ± 0.05	1.97 ± 0.06	1.31 ± 0.05	1.37 ± 0.05	1.20 ± 0.04
Nadk	5.22 ± 0.24	5.56 ± 0.22	4.34 ± 0.23	5.28 ± 0.17	3.73 ± 0.17	5.22 ± 0.25	3.89 ± 0.15	5.71 ± 0.33	5.02 ± 0.19	4.12 ± 0.20
FeA	1.00 ± 0.06	1.49 ± 0.10	1.05 ± 0.08	1.09 ± 0.08	1.27 ± 0.08	2.04 ± 0.11	1.00 ± 0.07	1.18 ± 0.08	1.47 ± 0.07	1.10 ± 0.08
FeB	1.13 ± 0.08	1.11 ± 0.10	−0.04 ± 0.03	0.59 ± 0.07	0.60 ± 0.08	1.24 ± 0.09	0.61 ± 0.06	0.30 ± 0.03	0.36 ± 0.04	0.26 ± 0.04
Cad	2.26 ± 0.11	1.81 ± 0.17	2.62 ± 0.16	−0.46 ± 0.20	3.60 ± 0.19	2.94 ± 0.11	1.48 ± 0.13	3.57 ± 0.14	3.28 ± 0.11	2.93 ± 0.12
Mg2k	1.15 ± 0.09	1.07 ± 0.11	0.62 ± 0.07	0.96 ± 0.05	0.52 ± 0.08	0.30 ± 0.05	1.52 ± 0.17	0.66 ± 0.06	0.80 ± 0.05	0.67 ± 0.05
CO12	23.48 ± 0.21	21.47 ± 0.27	18.42 ± 0.25	24.85 ± 0.33	20.40 ± 0.22	20.95 ± 0.18	23.22 ± 0.23	23.40 ± 0.26	23.26 ± 0.15	22.30 ± 0.20

Table 3. The equivalent widths in Å of the NIR line-strength indices of the sample galaxies with low SNR (< 100 $Å^{-1}$).

Index name	NGC 1600	NGC 3423	NGC 4415	NGC 7424
Pa1	-0.82 ± 0.28	0.56 ± 0.13	0.31 ± 0.05	0.25 ± 0.08
Ca1	0.98 ± 0.14	1.95 ± 0.16	1.28 ± 0.06	1.35 ± 0.10
Ca2	3.23 ± 0.09	3.97 ± 0.19	3.37 ± 0.07	3.51 ± 0.11
Ca3	3.07 ± 0.10	3.12 ± 0.08	3.13 ± 0.09	3.84 ± 0.14
Mgi	0.57 ± 0.08	0.28 ± 0.04	0.71 ± 0.05	0.48 ± 0.05
Ti	0.43 ± 0.07	1.02 ± 0.14	0.41 ± 0.15	0.35 ± 0.08
FeH	–	–	–	–
Paδ	–	–	–	–
FeTi	0.18 ± 0.05	–	–	–
CN	–	1.16 ± 0.10	0.16 ± 0.10	–
Sr	–	0.05 ± 0.10	-0.18 ± 0.06	0.14 ± 0.11
K1A	–	1.16 ± 0.20	1.11 ± 0.14	1.02 ± 0.33
k1B	–	0.30 ± 0.20	0.61 ± 0.12	1.73 ± 0.34
Mgj	1.46 ± 0.15	1.04 ± 0.11	–	–
Sij	1.15 ± 0.12	0.24 ± 0.15	0.53 ± 0.14	0.95 ± 0.23
SiMg	–	–	–	–
K2A	–	–	–	–
Paβ	1.45 ± 0.10	1.97 ± 0.29	–	3.03 ± 0.50
Al	1.99 ± 0.12	1.72 ± 0.16	0.86 ± 0.14	-0.10 ± 0.49
Mg1h	1.04 ± 0.35	2.05 ± 0.48	2.85 ± 0.24	–
Mg2h	4.19 ± 0.36	–	–	–
CO1	–	–	–	–
Br15	1.87 ± 0.62	1.53 ± 0.51	2.38 ± 0.29	–
Mg3h	5.86 ± 0.38	–	–	–
FeH1	2.25 ± 0.38	1.52 ± 0.46	2.15 ± 0.25	0.77 ± 0.78
Sih	3.32 ± 0.20	3.68 ± 0.45	4.17 ± 0.25	3.88 ± 0.76
CO2	3.44 ± 0.40	3.08 ± 0.23	–	–
CO3	4.57 ± 0.23	–	4.22 ± 0.23	5.19 ± 0.43
CO4	4.01 ± 0.13	1.93 ± 0.20	2.96 ± 0.25	2.76 ± 0.39
Fe3	–	–	1.71 ± 0.29	0.02 ± 0.35
Al1	4.56 ± 0.60	2.28 ± 0.18	3.98 ± 0.15	1.96 ± 0.26
COMg	–	3.85 ± 0.19	–	–
Br10	2.29 ± 0.16	1.29 ± 0.20	0.87 ± 0.20	–
MgIk	–	–	–	–
Nadk	–	–	–	–
FeA	–	–	–	–
FeB	–	–	–	–
Cad	–	–	–	–
Mg2k	–	–	–	–
CO12	–	–	–	–

index. We made a spline interpolation of the rms values as a function of broadening and considered this function as representative of the uncertainties associated with the correction coefficients relative to the line-strength index considered. The uncertainties in the index EW increase according to the multiplicative factor applied, as pointed out by Trager et al. (2000). For the total EW uncertainties, we also considered the uncertainties associated with the correction coefficients, which we added in quadrature to the intrinsic errors.

As the result of the velocity-dispersion correction, we identified three groups of NIR line-strength indices.

(i) The Ca2, Nadk, and CO12 indices are almost insensitive to the velocity-dispersion broadening, with a maximum variation with respect to the zero velocity-dispersion value smaller than 20 per cent at $\sigma = 400$ km s^{-1} (Cesetti et al. 2013). The rms of the correction coefficients is significantly small (< 10 per cent).

(ii) The Mg, Al, Si, and molecular line-strength indices, with the exception of a few TO line-strength indices, are very sensitive to the velocity-dispersion broadening, with a maximum variation with respect to the zero velocity-dispersion value larger than 50 per cent at $\sigma = 400$ km s^{-1} (Morelli et al. 2020), although the rms of the correction coefficients is small (< 20 per cent).

(iii) Many Fe and H line-strength indices are very weak and extremely sensitive to the velocity-dispersion broadening and the rms of the correction coefficients is very large (> 50 per cent).

We decided to investigate only NIR line-strength indices with SNR > 20 Å^{-1}, following Morelli et al. (2020), and to exclude from further investigation the following indices:

(i) Pa2, Pa3, Pa4, FeClTi, CSi, Paϵ, TiOA, TiOB, Fe, VO, Siy, Paγ, C, K2B, K1, Fe2, Br13, FeH2, Br11, FeI, since they have correction coefficients for the velocity-dispersion broadening with rms > 50 per cent;

(ii) FeCr, FeI, Brδ, Ca1k, Fe23, Sik, Ca2k, Ca3k, Ca4k, Pa5, Pa6, Na, and Brγ, which could be contaminated by telluric absorption and atmospheric emission;

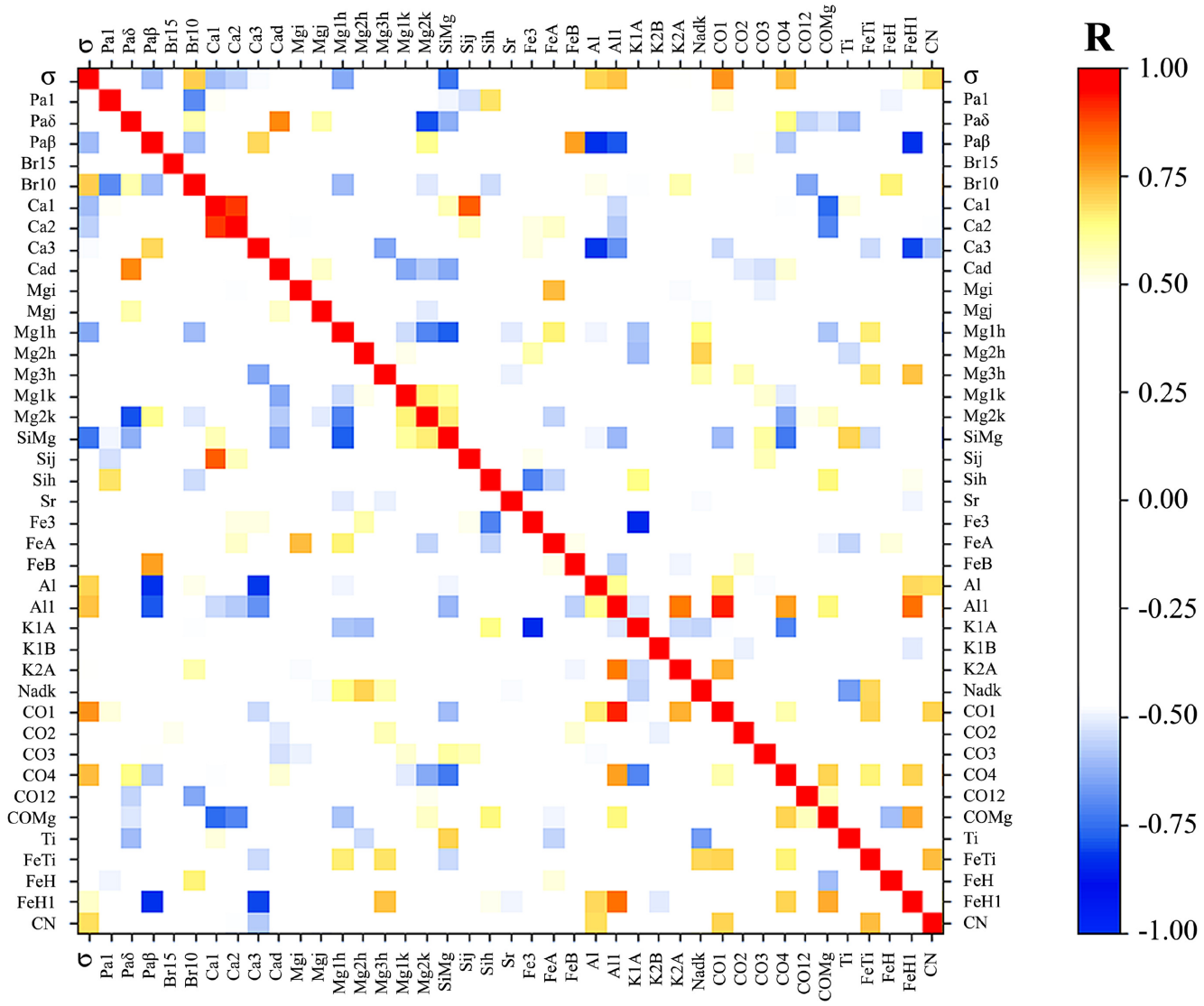

Figure 1. The correlation matrix for the final set of 40 NIR line-strength indices and velocity dispersions for the sample galaxies. Different colours correspond to different degrees of correlation according to Pearson statistics. For sake of clarity, only moderate and strong correlations and anti-correlations (with Pearson coefficient $0.5 < |R| < 0.7$ and $|R| > 0.7$, respectively) are shown. The correlations of the NIR line-strength indices with themselves and velocity dispersion with itself (giving $R = 1$ by definition) lie on the plot diagonal.

(iii) Br16 and CO5, because they are clearly contaminated by other spectral features.

The index denomination follows the definitions by Cesetti et al. (2013) and Morelli et al. (2020), which are based on the main element that produces the spectral feature. When more than one line-strength index is identified with the same name, we added a suffix that refers to the NIR band where it is observed. We did not detect NIR emission lines in any of the spectra of the sample galaxies.

3.2 Final set of indices

The final set of NIR line-strength indices contains 40 entries listed in Table 1.

We performed a visual inspection of the spectra of the sample galaxies and our conclusions are in line with previous works (e.g. Silva et al. 2008; Conroy & van Dokkum 2012; Röck et al. 2017; Alton, Smith & Lucey 2018) and can be summarized as follows.

(i) As expected (Alton et al. 2018), the strongest line-strength indices from molecular features are those related to the CO bands, in particular the CO12 index at 2.30 μm. The COMg index at 1.71 μm is the strongest non-CO molecular feature. Other molecular indices, like Ti, FeTi, CN, and FeH1 are weaker but still detectable. The FeH Wing–Ford index, a known gravity diagnostic (Schiavon, Barbuy & Singh 1997; Conroy & van Dokkum 2012), is very weak for almost all the sample galaxies, confirming the findings by Alton, Smith & Lucey (2017).

(ii) The strongest line-strength indices from atomic lines are those related to Ca, Mg, and Al, in particular the Ca1, Ca2, and Ca2 indices at ∼0.85 μm, Mg2h index at 1.50 μm, and Al1 index at 1.67 μm. The Nadk index at 2.20 μm and Sij index at 1.59 μm are remarkable features. The Fe line-strength indices are generally weak. The line

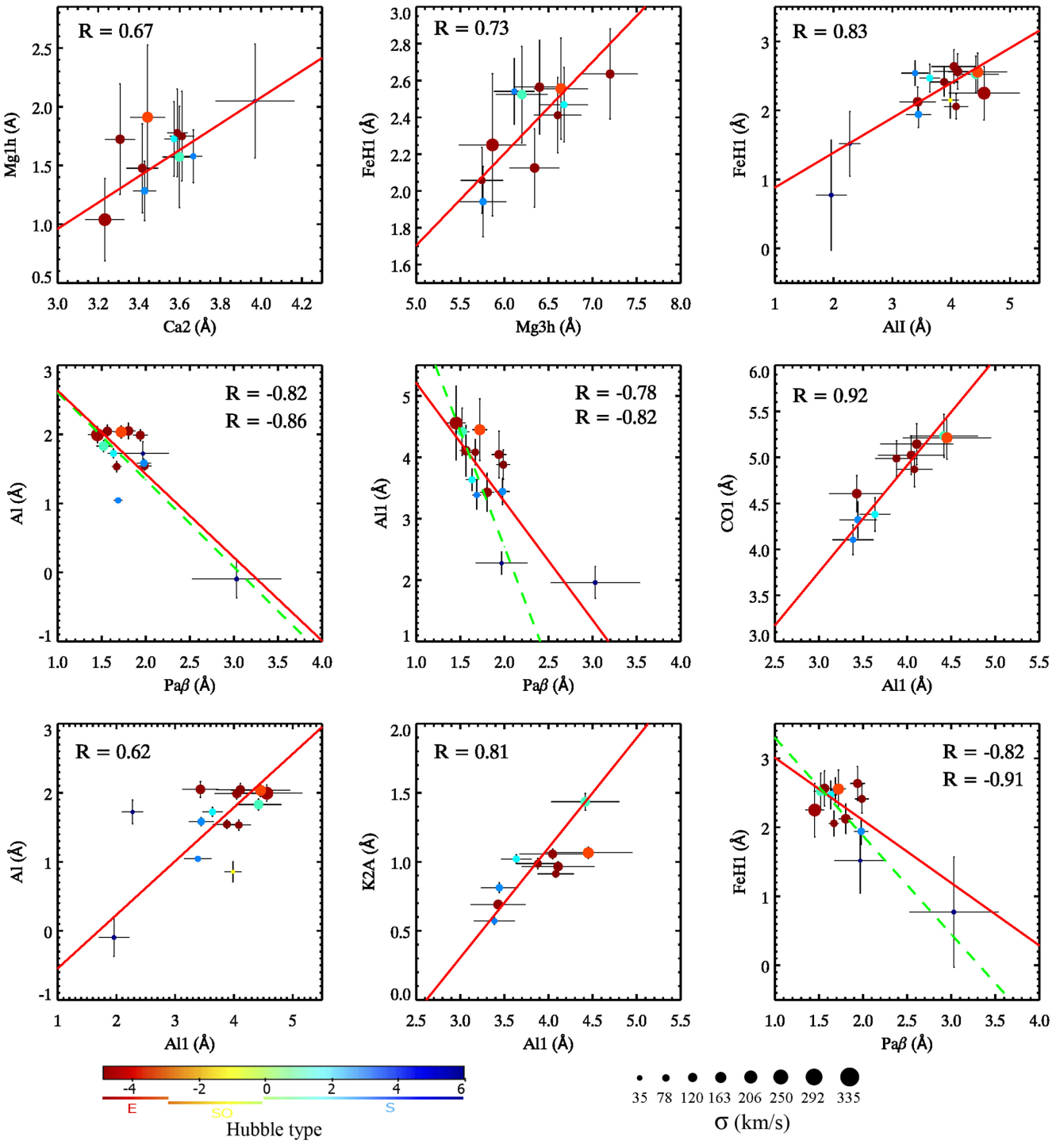

Figure 2. The stronger correlations between the NIR line-strength indices for the sample galaxies. Galaxies are colour-coded according to their Hubble type from the Lyon Extragalactic Database (Makarov et al. 2014). The size of each circle is proportional to the velocity dispersion of the galaxy. The best-fitting linear relations for all the sample galaxies (red solid line) excluding NGC 584, NGC 636, and NGC 2613 (green dashed line) are shown with their Pearson coefficient.

-strength indices from atomic lines in the *K* band are weak, but reside in a spectral region free of contamination.

(iii) Pa1, Paδ, and Paβ are the strongest indices among those related to hydrogen. Pa1 virtually disappears for NGC 1600 and NGC 3115 due to velocity-dispersion broadening, with a correction coefficient greater than 80 per cent. Therefore, the Pa1 EW for these two galaxies has to be considered with caution. The Br15 index is the strongest feature of the Brackett series, but it is always weaker than the Paschen indices. The Br10 index is very weak in all the sample galaxies.

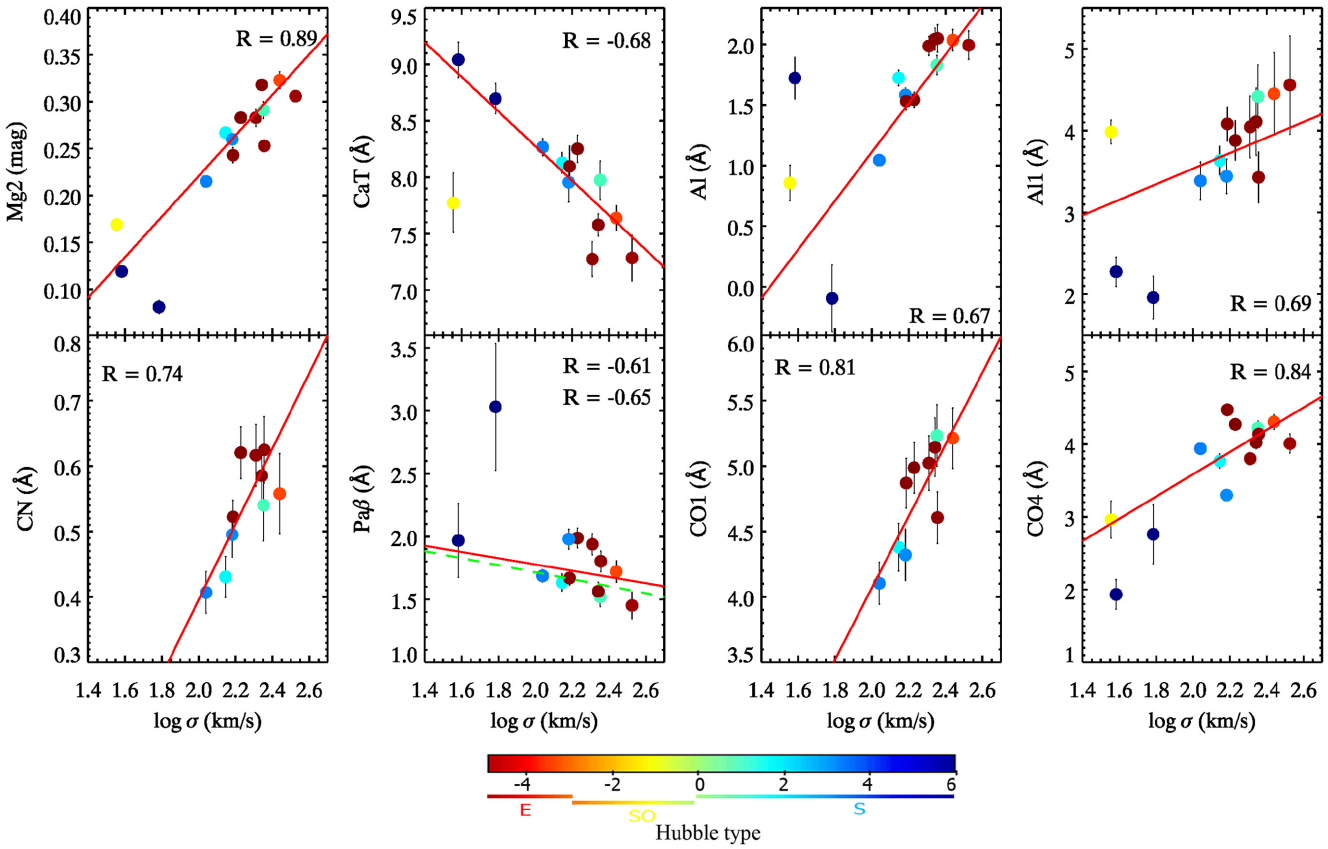

Figure 3. The stronger correlations between the NIR line-strength indices and velocity dispersion for the sample galaxies. The symbols are the same as in Fig. 2.

The EWs and corresponding uncertainties of the NIR line-strength indices measured with high accuracy for the sample galaxies are listed in Tables 2 (SNR $>$ 100 Å^{-1}) and 3 (SNR $<$ 100 Å^{-1}).

4 RESULTS

In this section, adopting a completely phenomenological approach, we present the properties of the NIR line-strength and their correlation with the velocity dispersion of the galaxies.

4.1 NIR–NIR correlations

We started correlating the NIR line-strength indices with each other to identify the most promising diagnostic of the properties of unresolved stellar populations. We adopted this approach with the twofold aim of investigating possible linear correlations between the NIR line-strength indices related to different elements and between NIR line-strength indices based on the same element. We performed a linear regression considering both X and Y uncertainties through the data points and we calculated their Pearson correlation coefficient R with the CORR Pearson function of the PANDAS[1] Python package.

Fig. 1 displays the correlation map for the final set of 40 NIR line-strength indices grouped by element with increasing wavelength. For visual purposes, we cut the colour scale to $|R| > 0.5$. We refer to a *moderate* correlation if $0.5 < |R| < 0.7$ and to a *strong* correlation when $|R| > 0.70$. The reddest and bluest squares mark the strongest correlations and anti-correlations, respectively.

The plot diagonal hosts the correlations of the NIR line-strength indices with themselves, which give a Pearson coefficient $R = 1$ by definition. To avoid spurious correlations due to large EW errors, we considered only those correlations with $|R| > 0.5$ for NIR line-strength indices with SNR $>$ 20 Å^{-1}, as done by Morelli et al. (2020). In some spectra, some line-strength indices do not pass the SNR threshold because they are contaminated by residuals of the subtraction telluric absorption and/or atmospheric emission, while, in the same spectra, other line-strength indices always have SNR $>$ 20 Å^{-1} (e.g. Paβ). Furthermore, we considered only the correlations that still hold with $|R| > 0.5$ when one random galaxy is removed from the analysis to account for the small-number statistics of our galaxy sample.

We found that only 20 out of the possible 780 correlations between NIR line-strength indices and velocity dispersion are strong, while about 100 correlations can be classed as moderate (Fig. 1). The strongest correlations between the NIR line-strength indices are shown in Fig. 2 and include the Mg1h–Ca2 and FeH1–Mg3h correlations already discovered by Riffel et al. (2019). In these cases, the slope and Pearson correlation coefficient obtained for our sample galaxies are consistent with those found by Riffel et al. (2019). The correlations between the Al1 and CO1 indices ($R = 0.92$) and between the Al1 and FeH1 indices ($R = 0.83$) are the strongest ones. The Paβ index does not show any strong correlation with any of the line-strength indices based on hydro-

[1]W. McKinney, PANDAS: a Python data analysis library, http://pandas.sourceforge.net

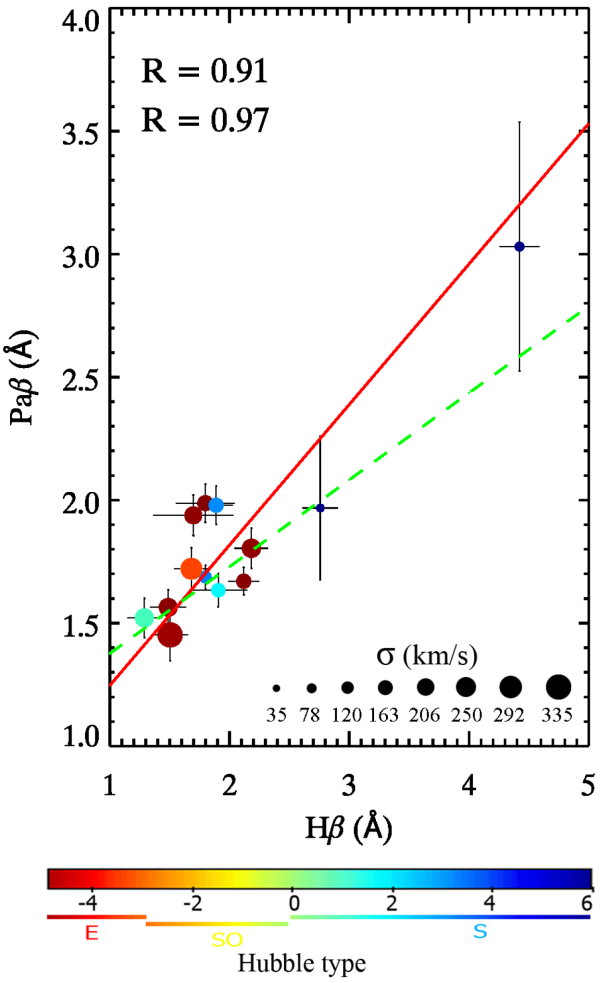

Figure 4. The correlation between the NIR Paβ index and optical Hβ index for the sample galaxies. The symbols are the same as in Fig. 2.

gen lines, which are in general very weak. On the other hand, the Paβ index correlates tightly with the Al and FeH1 indices (Fig. 2).

In Fig. 2 we also show the distribution of morphological types of the sample galaxies. We found that the EWs of metal line-strength indices (e.g. Al and FeH1) are larger for early-type galaxies and smaller for late-type ones (see also Riffel et al. 2019). NGC 3423 and NGC 7424 have a distinct behaviour with respect to the other sample galaxies, as they tend to lie in a separate region of parameter space. We suggest this is due to the fact that they are the only two late-type, low-velocity-dispersion, young and metal-poor galaxies of our sample (Paper I). Therefore, their stellar populations are different from those of the early-type galaxies that constitute most of our galaxy sample. For this reason, we considered these two galaxies interesting to unveil the global trends observed in line-strength indices moving from early to late-type galaxies. However, we are aware that this issue needs further investigation by increasing the number of young late-type galaxies.

4.2 NIR–σ correlations

In the optical regime, the correlation between some optical line-strength indices (e.g. Mg2, ⟨Fe⟩, and Hβ) and velocity dispersion was first found for early-type galaxies (e.g. Burstein et al. 1988; Bender, Burstein & Faber 1993; Bernardi et al. 1998; Mehlert et al. 2003) and then demonstrated to hold for late-type galaxies also (e.g. Moorthy & Holtzman 2006; Sánchez-Blázquez et al. 2006; Morelli et al. 2008). In the NIR domain, Cenarro et al. (2003) discovered a strong anti-correlation between the CaT index and velocity dispersion in the central regions of 35 early-type galaxies. Falcón-Barroso et al. (2003) found that this anti-correlation also holds for spiral bulges. Finally, the correlation between *K*-band line-strength indices (e.g. Na, Ca, and CO) and velocity dispersion was pointed out by Silva et al. (2008), Mármol-Queraltó et al. (2009), and Röck et al. (2017).

We investigated the correlation between NIR line-strength indices and velocity dispersions of the sample galaxies and show their Pearson coefficients in Fig. 1. We found that several NIR line-strength indices (Paβ, Br10, Ca1, Ca2, Mg1h, SiMg, Al, Al1, CO1, CO4, FeH1, and CN) show moderate-to-strong correlation with velocity dispersion. The strongest correlations between NIR line-strength indices and velocity dispersion are shown in Fig. 3.

We found that the Al and Al1 indices are tightly correlated with velocity dispersion, while the Paβ index shows a moderate anti-correlation with it. This trend resembles that observed for the Hβ index in the optical regime (Ganda et al. 2007; Morelli et al. 2008). Among the CO indices, the CO1 and CO4 indices display a stronger correlation with velocity dispersion. In the first and second panels of Fig. 3, correlations with the velocity dispersion are shown for optical Mg2 and CaT. Their trends are consistent with previous findings (Burstein et al. 1988; Cenarro et al. 2003).

5 AGE AND METALLICITY INDICATORS

In the previous sections, we found that some indices associated with metal elements do correlate with each other (e.g. Al, All, Paβ, CO1, FeH1). The linear correlation between these indices, in addition to the fact that their values are larger in more massive galaxies, as happens for metal indices in the optical regime (Sánchez-Blázquez et al. 2006; Morelli et al. 2008), is particularly interesting, since it suggests a connection between them and the metallicity of the galaxies.

In Section 4 we also found a trend between values of Paβ and the morphological types of the galaxies. Even if there are some notable exceptions, the old spheroids of ellipticals and early-types show, on average, lower values of Paβ with respect to the bulges of spiral galaxies (Figs 2 and 3). Since, in general, spheroids of ellipticals and early-types are older than the bulges of late-type galaxies, this result is a hint that Paβ could be a good candidate to trace the age of stellar populations.

To investigate better the possible uses for NIR line-strength indices such as age and metallicity indicators, we compared them with a set of optical indices known to be the best diagnostics of unresolved stellar populations in galaxies. We used the Hβ index as age indicator and ⟨Fe⟩, Mg2, Mgb, and [MgFe]′ (Thomas et al. 2003) as metallicity tracers. We measured their values for all the sample galaxies in Paper I.

5.1 Trends with age indicators

The Hβ index is widely used as an age indicator for unresolved stellar populations (e.g. Worthey et al. 1994; Lee, Yoon & Lee 2000). We expect that some of the line-strength indices based on H we studied could represent the NIR counterpart of the Hβ index. Except for Paβ, we did not find any strong trend with the Hβ index of the Pa1, Paδ, Br15, and Br10 indices. However, these indices as measured

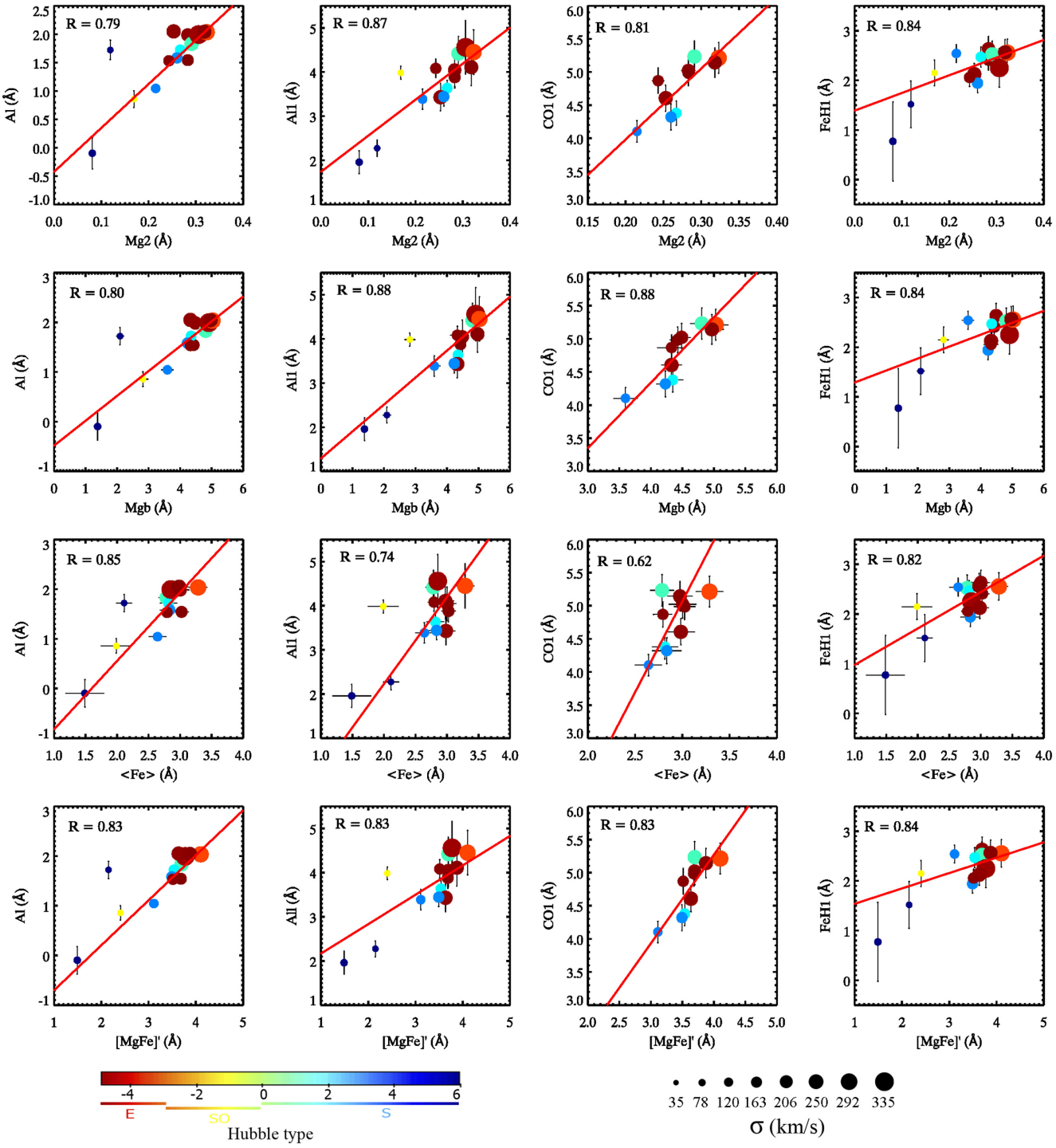

Figure 5. The correlations between the NIR Al, Al1, CO1, and FeH1 indices and optical Mg2, Mgb, ⟨Fe⟩, and [MgFe]′ indices for the sample galaxies. The symbols are the same as in Fig. 2.

in our spectra are too weak and/or contaminated by residuals of sky subtraction to allow robust comparisons with the Hβ index.

Fig. 4 shows the correlation between the Hβ and Paβ indices. This correlation is driven by the very young population resulting from the low SNR spectrum of NGC 7424 ($R = 0.91$), but it still holds ($R = 0.58$) if we do not consider this galaxy. In Fig. 4 we noticed that three galaxies seems to be shifted with respect to other sample galaxies, having a Paβ index ∼0.3 dex larger compared with galaxies of similar Hβ index. They are the Sb galaxy NGC 584 and the two elliptical galaxies NGC 636 and NGC 2613. They have an intermediate to high age ($T = 6$–10 Gyr) with supersolar metallicity ([Z/H] = 0.24–0.32 dex) and α/Fe enhancement ([α/Fe] = 0.20–0.25 dex). To investigate their behaviour further, we fitted a linear relation by excluding the three galaxies (Fig. 4). The Pearson coefficient improved from $R = 0.91$ to 0.97 and the correlation slope became slightly shallower, but it did not change the increasing trend of the Paβ index with the Hβ

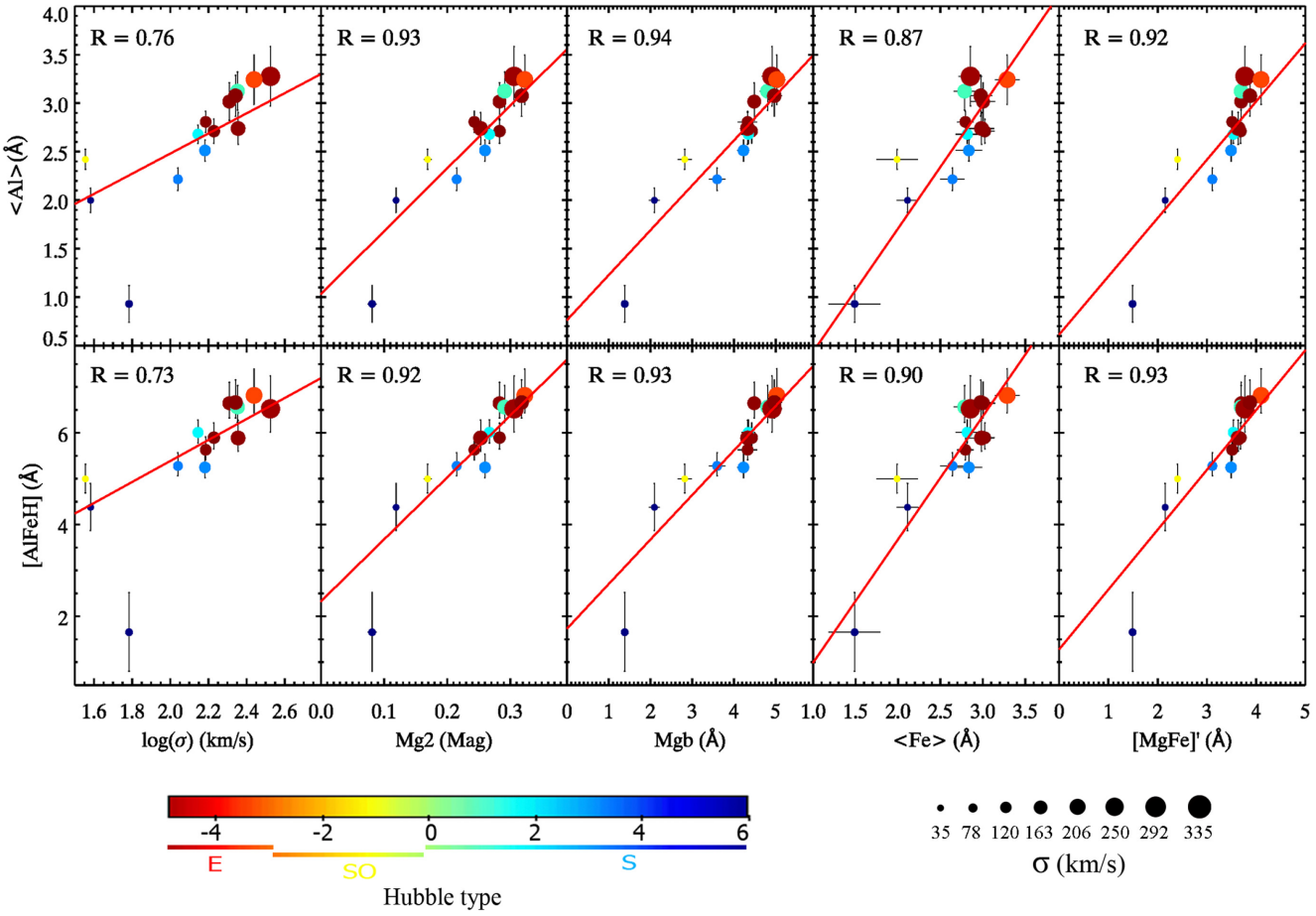

Figure 6. The correlations between the NIR ⟨Al⟩ and [AlFeH] NIR indices with velocity dispersion and optical Mg2, Mgb, ⟨Fe⟩, and [MgFe]′ indices for the sample galaxies. The symbols are the same as in Fig. 2.

index. We expect to strengthen this result and constrain the slope of the Paβ–Hβ relation better with more young galaxies in the high-end region of the Hβ index ($EW = 3$–5 Å).

5.2 Trends with metal indices

The optical Mg2 and Mgb indices are sensitive to α elements, while the ⟨Fe⟩ index is sensitive to the abundance of elements of the iron group. They are used to infer the total metallicity and α/Fe enhancement together with the [MgFe]′ index.

We found that none of the line-strength indices based on Fe for our NIR set shows a strong correlation with the ⟨Fe⟩ index, with the partial exception of two *K*-band FeA and FeB indices. However, considering the weakness of these lines, we preferred to focus our attention on the stronger FeH1 index.

In Fig. 5 we present the correlations between the Al, Al1, CO1, and FeH1 indices and the Mg2, Mgb, ⟨Fe⟩, and [MgFe]′ indices. The strongest correlations between the NIR and optical line-strength indices are the Al1–Mg2 ($R = 0.87$), Al1–Mgb ($R = 0.88$), CO1–Mgb ($R = 0.88$), and Al–⟨Fe⟩ ($R = 0.85$) correlations. The correlations between the Al1 and CO1 indices and the [MgFe]′ index are poorer with respect to those with the Mg2 index.

To improve the sensitivity of the NIR line-strength indices to the metallicity of the galaxies, we defined two new line-strength indices through linear combination of those available in our set. First, we considered line-strength indices due to the same element and for which Fig. 1 shows at least a moderate correlation with some of the optical indices. We did not find any notable improvement with either the Mg or CO indices, whereas we noticed that averaging the two Al indices into the combined ⟨Al⟩ index as

$$\langle \mathrm{Al} \rangle = 0.5(\mathrm{Al} + \mathrm{Al1}) \quad (1)$$

improved the correlations with the Mg2, Mgb, ⟨Fe⟩, and [MgFe]′ indices. We tightened these correlations further by including the FeH1 index to define the following combined [AlFeH] index:

$$[\mathrm{AlFeH}] = \mathrm{Al} + 0.5\mathrm{Al1} + \mathrm{FeH1}, \quad (2)$$

where we determined the 0.5 coefficient for the Al1 index empirically to maximize the correlation with the [MgFe]′ index.

Fig. 6 shows the correlations between the two composite indices with velocity dispersion and Mg2, Mgb, ⟨Fe⟩, and [MgFe]′ indices. These two newly defined line-strength indices are the most effective NIR indices to correlate with the optical metallicity indices. The ⟨Al⟩ index traces the behaviour of the Mg indices very well and maintains a strong correlation with the velocity dispersion, while [AlFeH] traces the behaviour of the ⟨Fe⟩ and [MgFe]′ indices better.

6 DISCUSSION

The Al and Al1 indices are among the strongest atomic features after the Mg indices and they show a behaviour similar to the Mgb and Mg2 indices. The origin of the only stable isotope of ^{27}Al is

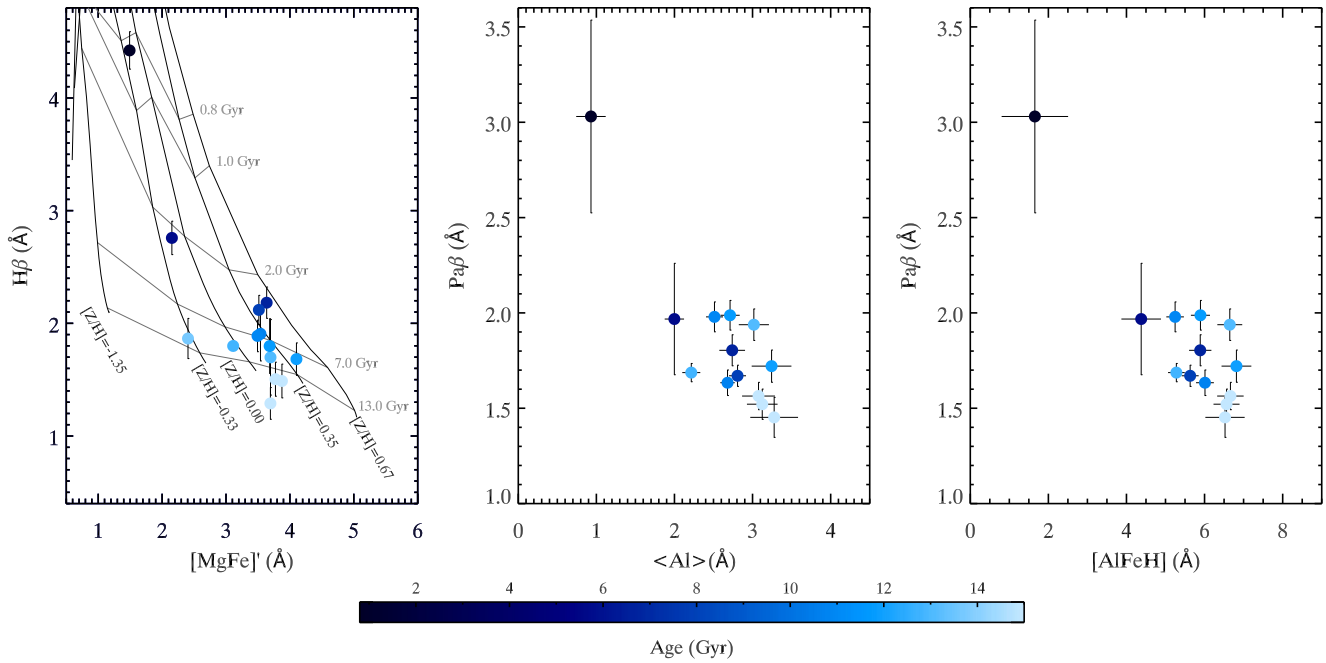

Figure 7. The distribution of measured values of the optical Hβ and [MgFe]$'$ indices (left panel), NIR Paβ and $\langle$Al$\rangle$ indices (central panel), and NIR Paβ and [AlFeH] indices (right panel) for the sample galaxies. The black and grey lines in the left panel correspond to the predicted values of the Hβ and [MgFe]$'$ indices for a grid of mean ages and total metallicities according to the models of Johansson et al. (2010) for an α/Fe enhancement of [α/Fe] = 0.3 dex. Galaxies are colour-coded according to their mean age.

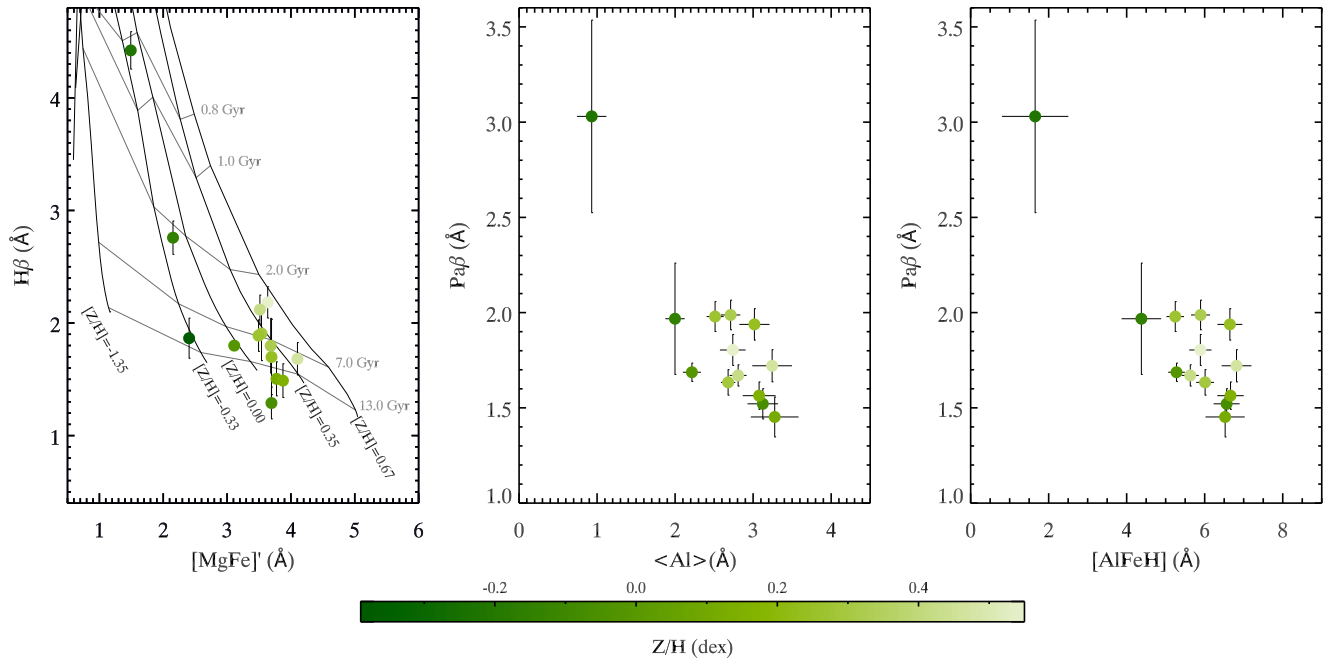

Figure 8. The distribution of measured values of the optical Hβ and [MgFe]$'$ indices (left panel), NIR Paβ and $\langle$Al$\rangle$ indices (central panel), and NIR Paβ and [AlFeH] indices (right panel) for the sample galaxies. The black and grey lines in the left panel correspond to the predicted values of the Hβ and [MgFe]$'$ indices for a grid of mean ages and total metallicities according to the models of Johansson et al. (2010) for an α/Fe enhancement of [α/Fe] = 0.3 dex. Galaxies are colour-coded according to their total metallicity.

still debated. According to Nordlander & Lind (2017), it can be produced in neutron-rich environments or via proton capture. In galaxies, the main sources may be SNII explosions and AGB stars, while SNIa explosions produce little or no aluminium. Pignatari et al. (2016) draw very similar conclusions and point out the fact that the production conditions for ^{27}Al are very similar to those for Mg. Considering also the correlation with the velocity dispersion (Fig. 3), the Al indices could be related to the formation

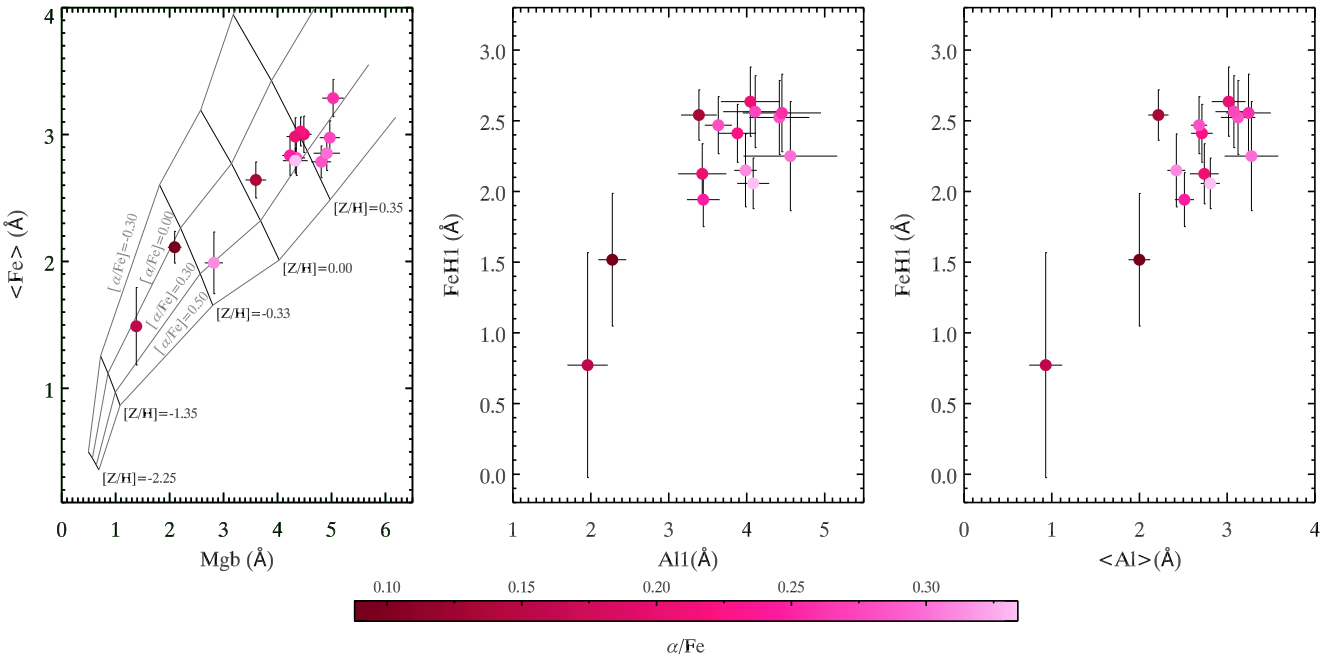

Figure 9. The distribution the measured values of the optical ⟨Fe⟩ and Mgb indices (left panel), NIR FeH1 and Al1 indices (central panel), and NIR FeH1 and ⟨Al⟩ indices (right panel) for the sample galaxies. The black and grey lines in the left panel correspond to the predicted values of the ⟨Fe⟩ and Mgb indices for a grid of total metallicities and α/Fe enhancement according to the models of Johansson et al. (2010) for a mean age of 7 Gyr. Galaxies are colour-coded according to their α/Fe enhancement.

and evolution of galaxies in the same way as the Mg2 and Mgb indices.

In the 0.8–2.5 μm range, there are only three iron features that might be used efficiently as metallicity diagnostics. The two *K*-band FeA and FeB indices have already been investigated (Silva et al. 2008), but they are weak and located in a spectral region of low SNR in the spectra of our sample galaxies. The FeH1 index is located in a spectral region relatively free from telluric and atmospheric features and not contaminated by other lines. In our sample galaxies, it is stronger than the FeH Wing–Ford band. For stars, the FeH1 index shows a dependence on surface gravity and metallicity (see figs D5 and D6 in Morelli et al. 2020). For galaxies, the strong correlations of the FeH1 index with the optical metal line-strength indices support the idea that it could be a good metallicity tracer.

The Paβ line is the strongest hydrogen feature for all the galaxies in our sample. We identified three galaxies, namely NGC 584, NGC 636, and NGC 2613, as possible outliers in the Hβ–Paβ relation (Fig. 4) and we tested their behaviour using the relations between the Paβ index and Al, Al1, and FeH1 indices (Fig. 2) as well as between the Paβ index and velocity dispersion (Fig. 3). Although in this case the three galaxies are difficult to identify as outliers, due to their small shift with respect to the bulk of the sample galaxies, we excluded them from the linear fit. The new best-fitting relations are also shown in Figs 2 and 3. The slope and Pearson coefficient are nearly the same for the Al–Paβ and σ–Paβ relations, while the slope is steeper for the Al1–Paβ and FeH1–Paβ relations but the trend is the same as before. We conclude that, with the actual number of galaxies and their distribution in parameter space, we cannot conclude firmly on the outlier nature of these galaxies.

The Paβ index does not suffer any significant contamination by other elements. Morelli et al. (2020) proved that the index behaviour in cool IRTF stars is driven by temperature, with no trends with surface gravity and metallicity. Cleri et al. (2020) showed that the Paβ index could be adopted as a tracer of the star formation rate in galaxies, showing a similar (and sometimes even better) behaviour with respect to the Hα and Hβ indicators. This supports our findings (Fig. 4) and it suggests that the Paβ index could also be considered as a good age tracer for unresolved stellar populations in the NIR.

We defined the ⟨Al⟩ and [AlFeH] indices to make stronger metallicity and α/Fe enhancement indicators available in the NIR. The ⟨Al⟩ index correlates tightly with velocity dispersion and optical Mg2 and Mgb indices (Fig. 6), in agreement with the theoretical findings of Pignatari et al. (2016) and Nordlander & Lind (2017). The [AlFeH] index is more sensitive to total metallicity, like the optical ⟨Fe⟩ and [MgFe]′ indices.

Considering the above correlation, we performed the following speculative analysis. In the left panels of Figs 7 and 8, the values of Hβ and [MgFe]′ of the sample galaxies (Paper I) are compared with the model predictions of Johansson et al. (2010) for a stellar population with supersolar α/Fe enhancement [α/Fe] = 0.3 dex. In this parameter space, the mean age and total metallicity of the galaxies are almost insensitive to variations of α/Fe enhancement. The sample galaxies are colour-coded according to their mean age (Fig. 7) and total metallicity (Fig. 8), which we derived in Paper I. For comparison, the values of ⟨Al⟩ and [AlFeH] of the sample galaxies are shown as functions of Paβ in the central and right panels of Figs 7 and 8. The distributions of data points in the ⟨Al⟩–Paβ and [AlFeH]–Paβ diagrams nicely match that of the [MgFe]′–Hβ diagram. Indeed, younger and more metal-poor galaxies lie in the upper left region, while older and more metal-rich galaxies are in the lower right region of all three diagrams. Both the ⟨Al⟩ and [AlFeH] indices are very effective in discerning the total metallicity compared with the [MgFe]′ index. For intermediate-age galaxies, the Paβ index seems slightly less efficient than Hβ in disentangling mean ages.

In the left panel of Fig. 9, the values of Mgb and ⟨Fe⟩ of the sample galaxies (Paper I) are compared with the model predictions

Table 4. The values of α/Fe enhancement for the sample galaxies estimated with the models of Johansson et al. (2010).

Galaxy	[α/Fe] (dex)
NGC 584	0.20 ± 0.07
NGC 636	0.22 ± 0.04
NGC 897	0.28 ± 0.11
NGC 1357	0.28 ± 0.04
NGC 1425	0.13 ± 0.04
NGC 1600	0.30 ± 0.08
NGC 1700	0.30 ± 0.05
NGC 2613	0.25 ± 0.06
NGC 3115	0.26 ± 0.02
NGC 3377	0.33 ± 0.07
NGC 3379	0.28 ± 0.11
NGC 3423	0.08 ± 0.08
NGC 4415	0.31 ± 0.10
NGC 7424	0.15 ± 0.06

of Johansson et al. (2010) for stellar populations with an intermediate age of 7 Gyr. In this parameter space, the total metallicity and α/Fe enhancement appear to be almost insensitive to variations in age. The sample galaxies in Fig. 9 are colour-coded by their total α/Fe enhancement, which we derived using a linear interpolation between the model points through the iterative procedure described in Morelli et al. (2008) and in Paper I. The values of α/Fe enhancement for the sample galaxies are reported in Table 4. For comparison, the values of Al1 and ⟨Al⟩ of the sample galaxies are shown as functions of FeH1 in the central and right panel of Fig. 9, respectively. The distribution of data points in the Al1–FeH1 and ⟨Al⟩–FeH1 diagrams matches that of the Mgb–⟨Fe⟩ diagram nicely. This is a promising result, although the absence of galaxies with extremely high/low values of [α/Fe] in our sample makes it difficult to evaluate the effectiveness of these NIR line-strength indices in constraining the α/Fe enhancement .

Following these results, we propose the NIR line-strength indices Paβ, ⟨Al⟩, Al1, FeH1, and, as possible counterparts of the optical indices, Hβ, [MgFe]$'$, Mgb, and ⟨Fe⟩ to investigate the unresolved stellar populations in the NIR domain for spectra with medium resolution ($R \sim 5000$) and high SNR (>100 Å^{-1}).

7 CONCLUSIONS

We investigated a set of 40 out of the 75 line-strength indices proposed by Cesetti et al. (2013) and Morelli et al. (2020) in the *I*, *Y*, *J*, *H*, and *K* bands for a sample of 14 nearby galaxies observed with the ESO XShooter spectrograph. The galaxies span the entire Hubble morphological sequence with a mean age range $0.8 \leq$ age $\leq$ 15 Gyr and a total metallicity range $-0.39 \leq$ [*Z*/H] ≤ 0.55 dex. Up to date, this is the largest set of line-strength indices measured and tested in the NIR domain.

We found that some of the NIR line-strength indices studied are promising candidates to constrain the properties of unresolved stellar populations in galaxies. To explore this idea further, we compared them with the most widely used optical age and metallicity indicators.

The Al, Al1, CO1, and FeH1 indices were found to be strongly correlated with the optical Mg2 and Mgb indices sensitive to α/Fe enhancement and with the ⟨Fe⟩ and [MgFe]$'$ indices sensitive to total metallicity. The Paβ index is tightly correlated with the Hβ index sensitive to mean age.

We defined two new combined indices ⟨Al⟩ and [AlFeH] to build stronger metallicity and α/Fe enhancement indicators in the NIR. The ⟨Al⟩ index correlates tightly with velocity dispersion and optical Mg2 and Mgb indices, while the [AlFeH] index is more correlated with the ⟨Fe⟩ and [MgFe]$'$ indices.

For our sample galaxies, we found a similar distribution of data points in the optical [MgFe]$'$–Hβ age–metallicity diagnostic diagram and in our two NIR counterparts given by the ⟨Al⟩–Paβ and [AlFeH]–Paβ diagrams. We also found a similar distribution of the data points in the optical α/Fe enhancement–metallicity diagnostic diagram and in our two NIR counterparts given by the Al1–FeH1 and ⟨Al⟩–FeH1 diagrams. This means that these new sets of NIR line-strength indices can be taken as a promising starting point to derive the mean age, total metallicity, and total α/Fe enhancement in unresolved galaxies.

Our next step of our work will be extending the galaxy sample to low ages (<5 Gyr) and to a broader range of metallicities. This will allow us to address better the differences in stellar populations of early-type galaxies and spiral bulges. This analysis can also be useful as a benchmark to test the new generation of NIR SSP model domains (e.g. Conroy & van Dokkum 2012; Röck et al. 2015, 2017; Vazdekis et al. 2016), which still require to be fine-tuned with observational data (Riffel et al. 2019).

ACKNOWLEDGEMENTS

EMC, EDB, and AP are supported by MIUR grant PRIN 2017 20173ML3WW_001 and Padua University grants DOR1885254/18, DOR1935272/19, and DOR2013080/20. LC acknowledges financial support from Comunidad de Madrid under Atracción de Talento grant 2018-T2/TIC-11612 and from Spanish Ministerio de Ciencia, Innovación y Universidades through grant PGC2018-093499-B-I00.

DATA AVAILABILITY

The reduced sample galaxy spectra used in this work have been presented and analysed in François et al. (2019). The reduced spectra are available upon request to the authors.

REFERENCES

Alton P. D., Smith R. J., Lucey J. R., 2017, MNRAS, 468, 1594
Alton P. D., Smith R. J., Lucey J. R., 2018, MNRAS, 478, 4464
Arentsen A. et al., 2019, A&A, 627, A138
Bender R., Burstein D., Faber S. M., 1993, ApJ, 411, 153
Bernardi M., Renzini A., da Costa L. N., Wegner G., Alonso M. V., Pellegrini P. S., Rité C., Willmer C. N. A., 1998, ApJ, 508, L143
Bica E., 1988, A&A, 195, 76
Bica E., Alloin D., 1987, A&A, 186, 49
Burstein D., Davies R. L., Dressler A., Faber S. M., Lynden-Bell D., Terlevich R., Wegner G., 1988, in Towards Understanding Galaxies at Large Redshift. Springer, Netherlands, p.
Cappellari M., Emsellem E., 2004, PASP, 116, 138
Cenarro A. J., Cardiel N., Gorgas J., Peletier R. F., Vazdekis A., Prada F., 2001, MNRAS, 326, 959
Cenarro A. J., Gorgas J., Vazdekis A., Cardiel N., Peletier R. F., 2003, MNRAS, 339, L12
Cesetti M. et al., 2009, A&A, 497, 41
Cesetti M., Pizzella A., Ivanov V. D., Morelli L., Corsini E. M., Dalla Bontà E., 2013, A&A, 549, A129
Cirasuolo M., Afonso J., Bender R., Bonifacio P., Evans C., Kaper L., Oliva E., Vanzi L., 2011, The Messenger, 145, 11
Cleri N. J. et al., 2020, preprint (arXiv:2009.00617)
Conroy C., van Dokkum P., 2012, ApJ, 747, 69
Costantin L. et al., 2019, A&A, 632, A9
Costantin L. et al., 2021, ApJ, 913, 125

Cuby J.-G. et al., 2010, in Ground-based and Airborne Instrumentation for Astronomy III. Proc. SPIE 7735, p. 933
Cushing M. C., Rayner J. T., Vacca W. D., 2005, ApJ, 623, 1115
Engelbracht C. W., Rieke M. J., Rieke G. H., Kelly D. M., Achtermann J. M., 1998, ApJ, 505, 639
Faber S. M., Friel E. D., Burstein D., Gaskell C. M., 1985, ApJS, 57, 711
Falcón-Barroso J., Peletier R. F., Vazdekis A., Balcells M., 2003, ApJ, 588, L17
François P., Morelli L., Pizzella A., Ivanov V. D., Coccato L., Cesetti M., Corsini E. M., Dalla Bontà E., 2019, A&A, 621, A60
Ganda K. et al., 2007, MNRAS, 380, 506
Gorgas J., Efstathiou G., Aragon Salamanca A., 1990, MNRAS, 245, 217
Guinouard I., Horville D., Puech M., Hammer F., Amans J.-P., Chemla F., Dekker H., Mazzoleni R., 2006, in Optomechanical Technologies for Astronomy. Proc. SPIE 6273, p. 1171
Ivanov V. D., Rieke G. H., Groppi C. E., Alonso-Herrero A., Rieke M. J., Engelbracht C. W., 2000, ApJ, 545, 190
Ivanov V. D., Rieke M. J., Engelbracht C. W., Alonso-Herrero A., Rieke G. H., Luhman K. L., 2004, ApJS, 151, 387
Johansson J., Thomas D., Maraston C., 2010, MNRAS, 406, 165
Jones J. E., Alloin D. M., Jones B. J. T., 1984, ApJ, 283, 457
Koleva M., Prugniel P., Bouchard A., Wu Y., 2009, A&A, 501, 1269
Kotilainen J. K., Hyvönen T., Reunanen J., Ivanov V. D., 2012, MNRAS, 425, 1057
Lee H.-c., Yoon S.-J., Lee Y.-W., 2000, AJ, 120, 998
Makarov D., Prugniel P., Terekhova N., Courtois H., Vauglin I., 2014, A&A, 570, A13
Mannucci F., Basile F., Poggianti B. M., Cimatti A., Daddi E., Pozzetti L., Vanzi L., 2001, MNRAS, 326, 745
Mármol-Queraltó E. et al., 2009, ApJ, 705, L199
McLean I. S., McGovern M. R., Burgasser A. J., Kirkpatrick J. D., Prato L., Kim S. S., 2003, ApJ, 596, 561
Mehlert D., Thomas D., Saglia R. P., Bender R., Wegner G., 2003, A&A, 407, 423
Mobasher B., Crampton D., Simard L., 2010, in Ground-based and Airborne Instrumentation for Astronomy III. Proc. SPIE 7735, p. 2106
Moorthy B. K., Holtzman J. A., 2006, MNRAS, 371, 583
Morelli L. et al., 2004, MNRAS, 354, 753
Morelli L. et al., 2008, MNRAS, 389, 341
Morelli L., Corsini E. M., Pizzella A., Dalla Bontà E., Coccato L., Méndez-Abreu J., Cesetti M., 2012, MNRAS, 423, 962
Morelli L., Calvi V., Masetti N., Parisi P., Landi R., Maiorano E., Minniti D., Galaz G., 2013, A&A, 556, A135
Morelli L., Pizzella A., Corsini E. M., Dalla Bontà E., Coccato L., Méndez-Abreu J., Parmiggiani M., 2015, Astron. Nachr., 336, 208
Morelli L., Parmiggiani M., Corsini E. M., Costantin L., Dalla Bontà E., Méndez-Abreu J., Pizzella A., 2016, MNRAS, 463, 4396
Morelli L. et al., 2020, A&A, 641, A44
Nordlander T., Lind K., 2017, A&A, 607, A75
Origlia L., Moorwood A. F. M., Oliva E., 1993, A&A, 280, 536
Origlia L., Ferraro F. R., Fusi Pecci F., Oliva E., 1997, A&A, 321, 859
Peletier R. F. et al., 2007, MNRAS, 379, 445
Pignatari M. et al., 2016, ApJS, 225, 24
Rayner J. T., Cushing M. C., Vacca W. D., 2009, ApJS, 185, 289
Riffel R. et al., 2019, MNRAS, 486, 3228
Robinson L. B., Wampler E. J., 1972, PASP, 84, 161
Röck B., 2015, PhD thesis. Instituto de Astrofisica de Canarias, Santa Cruz de Tenerife, Spain
Röck B., Vazdekis A., Peletier R. F., Knapen J. H., Falcón-Barroso J., 2015, MNRAS, 449, 2853
Röck B., Vazdekis A., Ricciardelli E., Peletier R. F., Knapen J. H., Falcón-Barroso J., 2016, A&A, 589, A73
Röck B., Vazdekis A., La Barbera F., Peletier R. F., Knapen J. H., Allende-Prieto C., Aguado D. S., 2017, MNRAS, 472, 361
Sánchez-Blázquez P. et al., 2006, MNRAS, 371, 703
Sarzi M. et al., 2006a, MNRAS, 366, 1151
Sarzi M. et al., 2006b, MNRAS, 366, 1151
Schiavon R. P., Barbuy B., Singh P. D., 1997, ApJ, 484, 499
Silva D. R., Boroson T. A., Elston R., Rich R. M., 1994, in Astronomy with Arrays, The Next Generation. Springer, Netherlands, p. 525
Silva D. R., Kuntschner H., Lyubenova M., 2008, ApJ, 674, 194
Thomas D., Maraston C., Bender R., 2003, MNRAS, 339, 897
Trager S. C., Faber S. M., Worthey G., González J. J., 2000, AJ, 120, 165
Vazdekis A., Sánchez-Blázquez P., Falcón-Barroso J., Cenarro A. J., Beasley M. A., Cardiel N., Gorgas J., Peletier R. F., 2010, MNRAS, 404, 1639
Vazdekis A., Koleva M., Ricciardelli E., Röck B., Falcón-Barroso J., 2016, MNRAS, 463, 3409
Villaume A., Conroy C., Johnson B., Rayner J., Mann A. W., van Dokkum P., 2017, ApJS, 230, 23
Worthey G., Ottaviani D. L., 1997, ApJS, 111, 377
Worthey G., Faber S. M., Gonzalez J. J., Burstein D., 1994, ApJS, 94, 687
Zibetti S. et al., 2017, MNRAS, 468, 1902

This paper has been typeset from a TEX/LATEX file prepared by the author.